GA–A26895

MAIN CHAMBER PLASMA-WALL INTERACTION STUDIES IN DIII-D IN SUPPORT OF ITER

by
J.G. WATKINS, D.L. RUDAKOV, C.J. LASNIER, A.W. LEONARD,
R.A. PITTS, J.H. YU, T.E. EVANS, R.E. NYGREN,
P.C. STANGEBY and W.R. WAMPLER

OCTOBER 2010

GENERAL ATOMICS

DISCLAIMER

GA–A26895

MAIN CHAMBER PLASMA-WALL INTERACTION STUDIES IN DIII-D IN SUPPORT OF ITER

by
J.G. WATKINS[1], D.L. RUDAKOV[2], C.J. LASNIER[3], A.W. LEONARD, R.A. PITTS[4], J.H. YU[2], T.E. EVANS, R.E. NYGREN[1], P.C. STANGEBY[5] and W.R. WAMPLER[1]

This is a preprint of a paper to be presented at the 23rd IAEA Fusion Energy Conference, October 11–16, 2010 in Daejon, Republic of Korea and to be published in Proceedings.

[1]Sandia National Laboratories, Albuquerque, New Mexico
[2]University of California-San Diego, La Jolla, California
[3]Lawrence Livermore National Laboratory, Livermore, California
[4]ITER, St Paul Lez Durance Cedex, France
[5]University of Toronto, Toronto, Ontario, Canada

Work supported in part by
the U.S. Department of Energy
under DE-AC04-94AL85000, DE-FG02-07ER54917,
DE-AC52-07N27344 and DE-FC02-04ER54698

GENERAL ATOMICS ATOMICS PROJECT 30200
OCTOBER 2010

ABSTRACT

Recent experiments in DIII-D have examined heat and particle flux profiles to main chamber regions that are of particular concern for the design of the ITER first wall. The first of these are at the high and low field side midplanes where ITER is expected to limit L-mode plasmas during the ramp-up and ramp-down phases of the plasma discharge. The scrape-off layer (SOL) power decay widths during inner wall limited (IWL) L-mode discharges in DIII-D are on the average ~2.5 times larger than those in diverted and upper outer wall limited plasmas for the same global parameters, in agreement with the assumptions used in the ITER first wall design. A second important area of concern for main chamber interactions in ITER is at the top of the vessel where a secondary divertor is expected to handle both steady state and ELMing levels of particles and energy. On DIII-D, measurements in H-mode show that the steady state heat flux deposition on this secondary divertor region is consistent with outer midplane power decay length scaling but the ELM energy deposition pattern is much more erratic, further away from the strike point, and in one ITER similar shape accounts for about 20% of the core ELM energy loss.

1. INTRODUCTION

Plasma facing components (PFCs) in ITER will have to withstand much higher incident fluences of particles and energy than those encountered in present day tokamaks. The power capabilities of the main divertor have been under study for some time based on an extensive database. One remaining first wall issue of particular concern and for which there is not much experimental data is the location and magnitude of heat flux falling on the vessel walls outside of the main divertor. The subject has been addressed in the ITER design through scrape-off layer models and models for ELM transport across flux surfaces. For this paper, we present experimental measurements from the DIII-D tokamak of the width of the primary power scrape-off length during plasma startup on the limiters and the magnitude and distribution of power deposited in the secondary diverter both in steady state and during ELMs.

2. TESTS OF ITER LIMITER L-MODE SOL POWER WIDTH SCALING

Plasma start-up and ramp-down in ITER will use limiter configurations. The ITER first wall (FW) is being designed to allow startup on the actively cooled beryllium panels on both the high (HFS) and low (LFS) field sides, and plasma control scenarios have been developed [1]. Here we report results of a dedicated experiment performed in the DIII-D tokamak that validate the key assumptions used to design the FW for power handling during limiter operation.

The power handling capacity is determined by the parallel heat flux density, $q_{\|}$ and the FW panel shaping. The profile of $q_{\|}$ is characterized by the scrape-off layer (SOL) power flux density e-folding length, λ_q. In the ITER Thermal Load Specifications [1,2] which form the design basis for the FW and divertor PFCs, λ_q in L-mode divertor phases is estimated assuming the scaling derived from measurements of divertor target power fluxes mostly from JT-60U and JET (with an uncertainty of a factor of ~2 around this value):

$$\lambda_q\,(\mathrm{m}) = (1\pm1/3)\; 3.6\; 10^{-4}\; \mathrm{R}\,(\mathrm{m})^2\; P_{\mathrm{div}}\,(\mathrm{MW})^{-0.8}\; \mathrm{x}\; q_{95}^{0.5}\; \mathrm{x}\; \overline{n}_{\mathrm{e}}\; (10^{19}\,\mathrm{m}^{-3})^{0.9}\; \mathrm{x}\; Z_{eff}^{0.6}\quad , \qquad (1)$$

where R is the major radius, P_{div} is the conducted power to the divertor, $\overline{n}_{\mathrm{e}}$ is the line averaged plasma density and Z_{eff} is the plasma effective charge. In the absence of a similar scaling for limiter plasmas, Eq. (1) has been applied to estimate λ_q for the limiter ramp-up/down phases in ITER by replacing P_{div} by the power to the limiters and taking into account the effect of a variable number of poloidal limiters following the model in Ref. [3].

Experimental measurements in tokamaks show considerably larger SOL width in HFS- compared to LFS-limited configurations ([4] and references therein). This is explained by the strong ballooning component of edge transport in tokamaks, which leads to larger SOL widths when plasmas are limited on the HFS. As a consequence, the value of λ_q mapped to the outboard midplane is usually expected to be ~2.5x larger in HFS limiter plasmas than in their LFS counterparts [3]. When flux expansion is taken into account, the local value of λ_q at HFS in ITER is expected to be ~4x larger than that on the LFS [2]. For given power into the SOL (P_{SOL}), this increase over-compensates the increased parallel power flux (due to the stronger toroidal field on the HFS) and makes HFS start-up advantageous compared with LFS configurations. There are in fact several other advantages to HFS start-up [1], so it is important to confirm that these ITER assumptions for limiter power loading are correct. Here we report results of the recent λ_q measurements in DIII-D performed in both HFS-limited (inner-wall-limited, IWL) plasmas of varying elongation, and lower single null (LSN) diverted discharges. A single discharge with the plasma limited at the top of the vessel was also executed as an approximation to LFS-limited conditions, for which the DIII-D FW is not optimized.

A poloidal cross-section of DIII-D together with the shapes of the last closed flux surface (LCFS) in configurations used in this study are shown in Fig. 1. Figure 1(a) includes two IWL configurations with slightly different elongation, $\kappa\sim1.4$ and $\kappa\sim1.5$. It is worth noting that δ, the distance between the top of the LCFS and the toroidally continuous "knee limiter" decreases with the increasing elongation. Figure 1(b) shows the separatrix in LSN and the LCFS of top-limited (TL) discharges along with the poloidal location of the midplane reciprocating probe array (RCP) and the field of view of the infrared camera (IRTV). The RCP is used to determine the e-folding lengths, λ_n and λ_T of n_e and T_e in the LFS SOL. Assuming $T_i = T_e$ (since T_i measurements are unavailable) and sheath-limited heat flux, $q \propto n_e T_e^{3/2}$ allows λ_q to be computed as $1/\lambda_q = 1/\lambda_n + 3/2\lambda_T$. The IRTV measures the heat flux profile across the lower divertor floor that is compared with the probe measurements of λ_q in the LSN configuration.

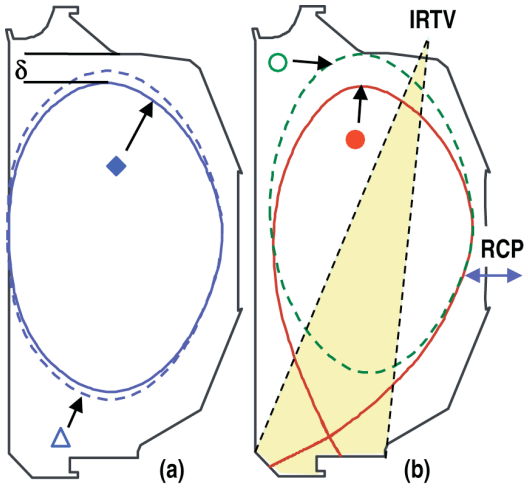

FIG. 1. Poloidal cross-sections of the LCFS in the magnetic configurations used in the study and diagnostic arrangement.

The experiment comprised a series of ohmic and neutral beam injection (NBI) heated L-mode discharges. Profiles of n_e and T_e were measured with the RCP twice per discharge, at $t = 2.5$ s and $t = 3.5$ s. Plasma current and density were scanned from shot to shot, while NBI heating power, P_{NBI}, was increased stepwise in some of the discharges from 0 to 1.25 MW at $t = 3.0$ s. The scaling parameters in Eq. (1) were varied in the following ranges: $q_{95} = 3.2$–7.4, $\bar{n}_e = 1.1$–$4.5\times10^{13}\,\mathrm{cm}^{-3}$, $P_{SOL} = 0.1$–1.4 MW. Here P_{SOL} is used in place of P_{div} in Eq. (1) and is calculated as the sum of ohmic and NBI heating power minus the power radiated from the plasma core. There was no systematic change in core impurity concentration throughout the scans with $Z_{eff} \sim 2$ in all discharges. We should note that it was not possible to change the scaling parameters independently. For example, an increase in the heating power typically resulted in an increase in the plasma density.

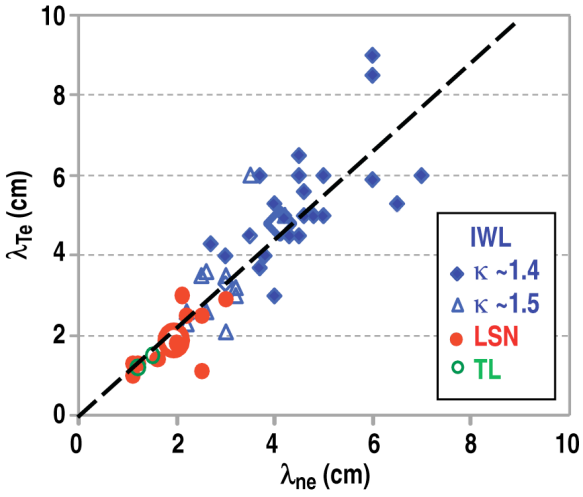

FIG. 2. Correlation between density and temperature e-folding lengths.

The full data set consists of 37 IWL, 10 LSN and 2 TL profiles. Figure 2 plots λ_T versus λ_n for all useable profiles in the dataset. A few profiles were discarded because the probe reciprocations did not allow close enough approach to the LCFS and/or due to excessive

scatter in the raw data, resulting in poor fits. There is a good correlation, with $\lambda_T \sim 1.1\ \lambda_n$ on average (dashed line). The large open symbols show averages across the dataset for IWL (diamond) and LSN (circle) configurations, clearly demonstrating that in the IWL configuration, both λ_T and λ_n are ~2.5 times larger than in LSN and directly confirming one of the key ITER limiter load spec assumptions. The two available TL profiles have λ_T and λ_n comparable to LSN values (somewhat smaller than the LSN average), indicating that the ITER use of a modified divertor scaling law for limiter discharges has some validity.

In order to check the validity of the derivation of λ_q from the probe data, IRTV was used in LSN discharges to compare with the probe derived results. Out of 10 LSN profiles, 3 were obtained with the outer strike point (OSP) detached, and IRTV data could not be used. Six out of the remaining seven profiles show agreement to within a factor of 2 between λ_q values from IRTV (mapped to the LFS midplane) and the probe, which is reasonable within the measurement uncertainties.

A comparison of the λ_q values derived from probe data of Fig. 2 with those calculated using the scaling in Eq. (1) is shown in Fig. 3(a) for the entire usable dataset, where, the IWL data have been scaled down by a factor of 2.5 to be comparable with LSN data and the scaling assumptions. It is evident from this comparison that our results do not confirm the assumed parametric dependence of the ITER λ_q scaling. However, the overall disagreement in absolute values is not very large. Moreover, not all experimental points may be suitable for comparison with the scaling. Equation (1) assumes attached conditions, while some of the higher density and lower I_p (higher q_{95}) discharges may have been detached. We do not have a good indication for detachment in IWL discharges, but those which are radiation-dominated (with low P_{SOL}) are likely to be detached. For LSN discharges IRTV data confirm that those with $P_{SOL} < 0.25$ MW are detached. In addition, a clear correlation was found between λ_q and δ, the distance between LCFS and the "knee limiter" (Fig. 1), with λ_q in higher κ, lower δ discharges being on the average ~30% lower than in lower κ, higher δ cases. Therefore, we conclude that proximity of the secondary limiter to the LCFS may affect the SOL width in higher κ discharges and that data from those discharges is not likely to be

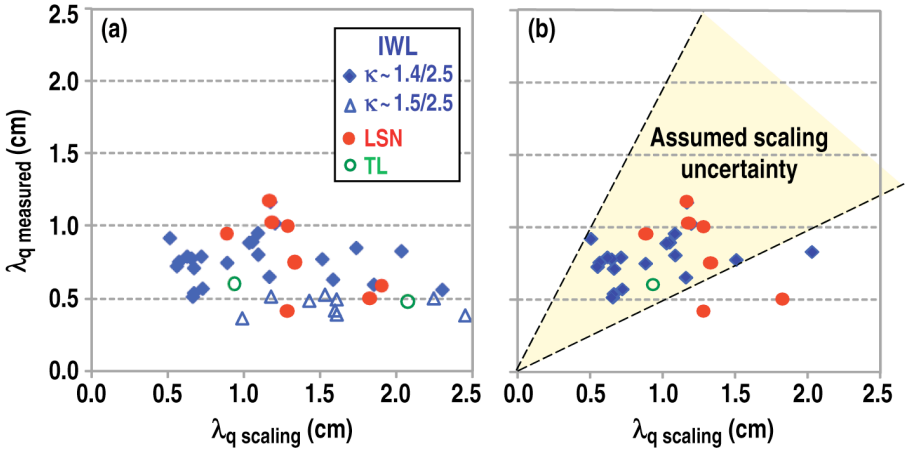

FIG. 3. Comparison of the measured heat flux e-folding length (reduced by a factor of 2.5 for the IWL points) with assumed ITER scaling of Eq. (1) over full dataset (a) and with questionable points removed (b).

suitable for comparison with the scaling of Eq. (1). Points with $P_{SOL} < 0.25$ MW and higher elongation have therefore been removed from Fig 3(b). All but one remaining IWL point and most LSN points (except for two with $P_{SOL} \sim 0.3$ MW that are close to detachment) agree with the scaling within the assumed uncertainty factor of 2.

The primary goals of our experiments were to benchmark the ITER SOL power width scaling of Eq. (1) in both limited and diverted configurations and demonstrate the larger λ_q for HFS versus LFS limiter configurations. Three of five scaling parameters (q_{95}, $\overline{n}_e$ and P_{SOL}) were varied in a rather wide range, although they do not vary independently and it is thus impossible with this dataset to check the individual scaling dependencies of Eq. (1). Moreover, the measured λ_q values show no correlation with the scaling trends as the plasma parameters change. On the other hand, with the exception of detached discharges and those affected by a proximity of the secondary limiter, the absolute measured values of λ_q agree with the scaling within the assumed uncertainty of a factor of 2. This result provides some confidence that the scaling relationship may be a reasonable assumption provided that the FW design accounts adequately for the uncertainty. The strongest dependence of the scaling in Eq. (1) — the one on the major radius — could not be directly tested in our experiments. However, the fact that our results are in reasonable agreement with a scaling based on data from JT-60U and JET, machines with a considerably larger R, constitutes an approximate confirmation of the validity of the R^2 dependence in Eq. (1). This is an important result, greatly increasing the confidence in the application of Eq. (1) to ITER.

3. PMI IN THE SECONDARY DIVERTOR

ITER will use unbalanced double-null configurations for which a secondary divertor region exists at the top of the vessel and for which first wall design must account. Power fluxes in this region have not been well diagnosed and thermal and particle loads during and between ELMs need to be better characterized in support of the proposed ITER first wall design. Detailed measurements of the ELM energy and particle deposition footprint on the secondary divertor target plates were made with a fast IR camera, Langmuir probes, and fast response thermocouples embedded 1 cm below the target plate surface. We studied the effect of density and magnetic balance on the heat flux distribution in the secondary divertor. The magnetic balance is quantitatively described by DRSEP, the distance between the primary and secondary separatrix at the outer midplane.

The most illustrative diagnostic for this study was the IRTV: images of the secondary divertor before and during an ELM are shown in Fig. 4. The ELM image intensity has been reduced in the right picture to better show the deposition pattern. For the quantitative study of heat flux profiles in this paper, surface temperature profiles were measured at 12 kHz in line scan mode using a 496x4 pixel profile with an 8 μs integration time. Surface temperature profiles were converted to heat flux using the THEODOR code [5]. The THEODOR code uses a model for thin surface layers where layer thickness was adjusted to keep the calculation of heat flux from going negative just after an ELM. The layer model, to be more realistic, needs to use different thickness layers at different locations but so far this refinement has not been incorporated into the calculation. Steady state heat flux results were compared with fast thermocouple measurements in order to validate the heat flux measurements. Some example cases demonstrated agreement within 20% for steady state, long pulse, non-ELMing exposures.

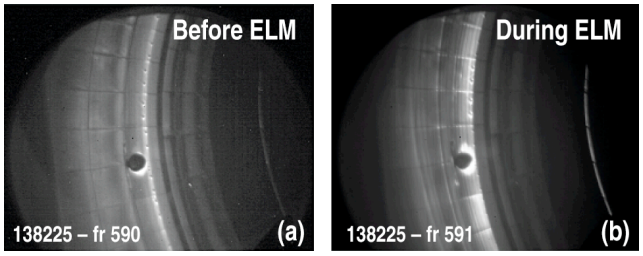

FIG. 4. Fast IR camera images of the secondary divertor before and during an ELM.

One difficulty with making IRTV measurements in the secondary divertor was the possible presence of both specular and diffuse reflections of the brighter primary divertor heating pattern seen at the secondary divertor targets particularly during ELMs. The diffuse background radiance was dependent on overall image brightness and therefore particularly significant during ELMs. Techniques were developed to reduce the impact of background infrared emission light on the ELM energy deposition measurements. The background removal technique involved subtracting a fitted quadratic background profile from each heat flux profile. The background was fit to the main profile over the private flux region and at the edges of the field of view where the heat flux is expected to be very small. This technique is preliminary but provides an upper limit on ELM energy deposition to be established for the

secondary divertor. Any improvement in the background subtraction would only produce a lower heat flux than the present technique. Also, due to motion of the camera in some cases, it will be necessary in the future to implement a spatial correction of the temperature profiles before calculating the heat fluxes. This effect is more significant at the ISP but mostly cancels out for the time-averaged cases at both strike points.

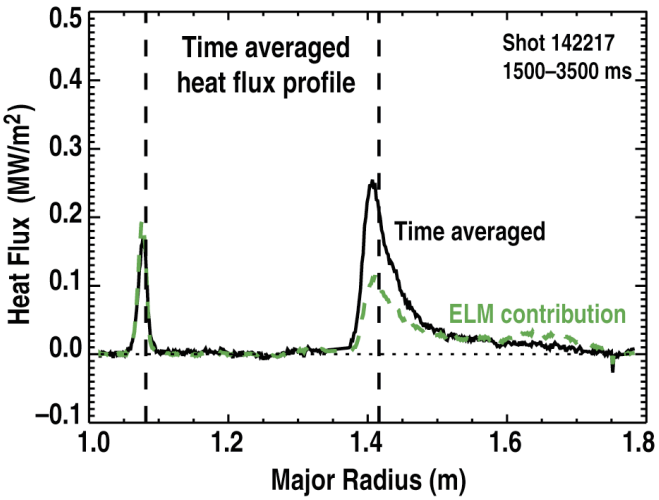

FIG. 5. This time-averaged heat flux profile with background subtracted has been averaged over 2 seconds. The two vertical dashed lines indicate the predicted location of the strike points in the secondary divertor. The ELM footprint (dashed green line) shows a peak near the secondary divertor strike point and is broader than the time-averaged profile. The time-averaged heat flux at the inner strike point is largely due to ELMs. The outer SOL bump (dashed line) is partially an artifact of extra surface layers in the far SOL.

Steady state heat flux profiles averaged over ELMs show that the footprint in the secondary divertor is peaked at the secondary strike point with an exponential spatial decay as shown in Fig. 5. Averaged over ELMs, λ_q in the secondary divertor is observed to be consistent with midplane power width scaling derived from IRTV measurements at the primary divertor [6]. This scaling predicts $\lambda_q = 0.7$ cm/I_p (MA) = 0.6 cm for the case shown in Fig. 5. The (1/e) decay length measured in the heat flux profile shown in this figure is 4.9 cm and, with a flux expansion of 7.5, represents a decay length of 0.65 cm at the outer midplane for the 1.18 MA case shown. Integrating just the ELM deposited energy over the 2 s averaging window yields the time-averaged ELM contribution to the heat flux profile which is also shown in Fig. 5. The ELM frequency for this case is about 20 Hz. Therefore, the heat flux profile near the strike point in the secondary divertor, for this shape with DRSEP ~0.8 cm, is consistent and predictable from the primary divertor power scaling. Figure 5 also indicates that most of the heat deposits onto the target plate between ELMs at the outer strike point and during ELMs at the inner strike point and far SOL. By spatially integrating the time-averaged profile shown in Fig. 5, the secondary divertor is found to receive about 5% of the total power coming across the separatrix.

The secondary target plate heat flux footprint from individual ELMs is not as predictable and well behaved as the time-averaged case. For many of the ELMs, we have observed large heat flux peaks more than 20 cm away from the secondary strike points and the heat deposition pattern is not well described by a simple mathematical function. An example of this type of profile is shown in Fig. 6. It was found that the ELM deposition pattern was not regularly correlated with the expected locations for reflected upper divertor signals and therefore is assumed to be real incident heat flux. The heat flux levels shown here have been reduced using the quadratic background subtraction described earlier. The ELM heat flux

levels are typically 20–40 times higher than steady state levels but only last for 1–2 ms. The profiles shown in Fig. 6 are measured at 12 kHz during an ELM.

Averaged over many ELMs, a more regular heat flux pattern emerges as shown in Fig. 5. The averaged ELM footprint is peaked at the strike point and broader than the narrower steady state heat flux profile between ELMs. Approximately half of the heat flux at the secondary strike point is due to ELMs. This fraction increases to nearly all of the observed heat flux farther than 10 cm from the strike point. The ELM contribution larger than the time-averaged profile in the far SOL of Fig. 5 ($R > 1.6$ m) is likely an artifact of radially varying surface layers that have not yet been adequately taken into account. The fraction of particle flux to the secondary divertor due to ELMs has a similar profile to that of the heat flux. Shown in Fig. 7 is the target plate Langmuir probe measurements of the ELM particle flux normalized to the total time-averaged divertor particle flux. The shape of this profile shows that the majority of particle flux further out in the scrape-off layer comes from ELMs but extrapolating the curve back to the strike point indicates the ELMs contribute somewhat less than 50% of the total time-averaged particle flux at the strike point.

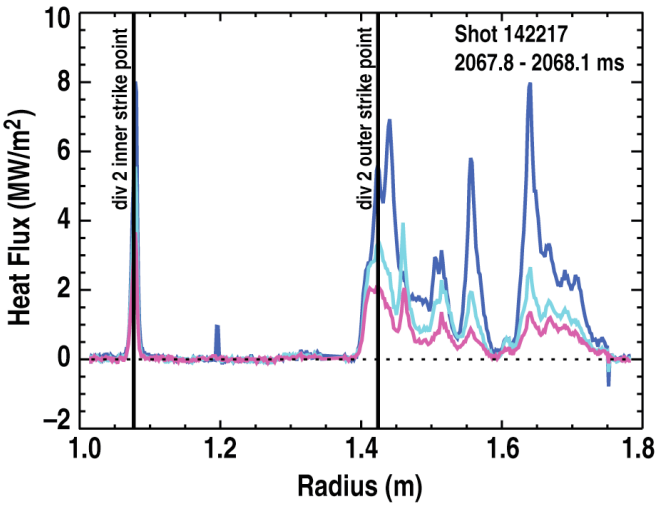

FIG. 6. The ELM heat flux footprint is shown for three different times during the ELM. The shape is variable and could be affected by reflections but the ELM time is short compared to the steady state heating time. Notice that the amount of heat flux at the inner strike point is larger than expected for the secondary divertor. It is unexplained how significant levels of heat can reach the inner strike point of the secondary divertor.

The fraction of energy deposited in the secondary divertor during ELMs has been measured to be about 20% of the core energy loss for the ITER similar shape but this fraction depends on both DRSEP and density. The target deposited energy is determined by integrating the heat flux profile over the entire divertor assuming toroidal symmetry and over the ELM deposition time of a few

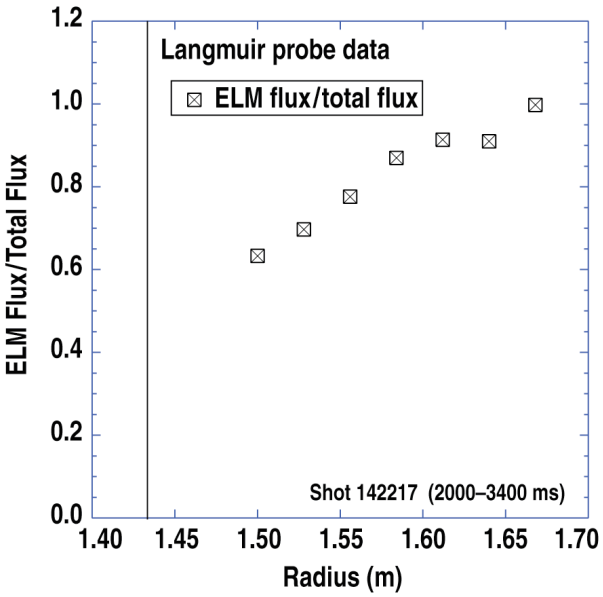

FIG. 7. Each point plotted represents a target plate Langmuir probe location. The fraction calculated is the integrated particle flux at each probe during ELMs/total flux to the probe including ELMs. This shows that the ELM footprint is broader than the steady-state profile.

milliseconds. The integrated ELM delta E is shown in Fig. 8 for a 2000 ms window (95 ELMs). The core delta E energy loss per ELM is determined from a fast equilibrium calculation using the EFITD65Y equilibrium code. The fraction of total core ELM energy loss going to the secondary divertor is shown in Fig. 9 and the median value for this case is 21%. This fraction of ELM energy deposited on the secondary divertor target plates (21%) is expected to be larger than the fraction of steady state heat flux deposited there (5%) because the ELMs reach further out past the main separatrix and put more energy into the secondary SOL and divertor. This also results in a broader footprint in the time-averaged heat flux profile as shown in Fig. 5. Another interesting feature of the secondary heat flux profile is that the inner strike point heat flux levels are significant and due almost entirely to ELMs. This feature was unexpected and the mechanism is as yet unexplained as the inboard strike-point is not magnetically connected to the outboard SOL where ELMs are thought to originate. If subsequently verified, this secondary inner strike-point heat flux will have to be accounted for in first wall design.

One encouraging observation during the secondary divertor study was that both the density and the magnetic balance (DRSEP) can be used to reduce steady state heat flux and ELM energy deposition in the secondary divertor. The three profiles in Fig. 10 show the effect of increased density and increased DRSEP on the resulting heat flux footprint. For an ITER similar shape with the ion $B \times \nabla B$ drift towards the primary upper X-point, 33% larger core plasma density ($5.5 \rightarrow 7.3 \times 10^{19}$ m^{-3}) resulted in smaller ELMs, less radial transport of particles, and 44% less peak heat flux and 60% less energy per ELM into the secondary SOL and divertor. As the magnetic balance shifts more towards the main divertor, the heat and particle flux to the secondary divertor is reduced and the total energy per ELM deposited on the secondary divertor drops proportionally with DRSEP.

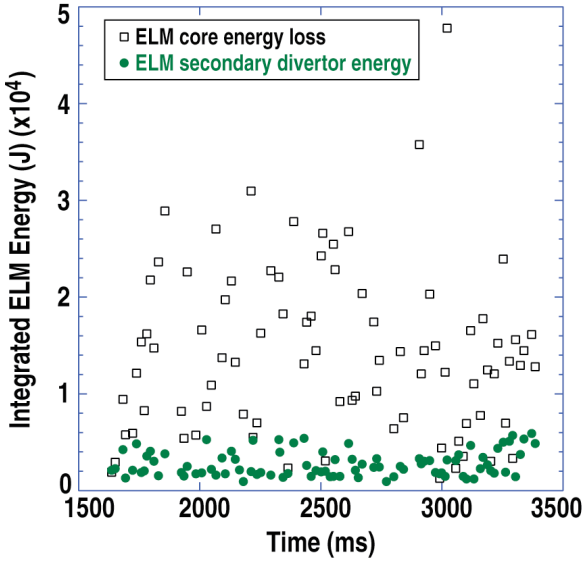

FIG. 8. The figure shows both the total integrated core ELM energy loss (squares) and the secondary divertor total ELM energy deposition (dots). There is considerably more uncertainty in the lower core ELM energy values which influences the fraction of energy deposition calculated in the secondary divertor.

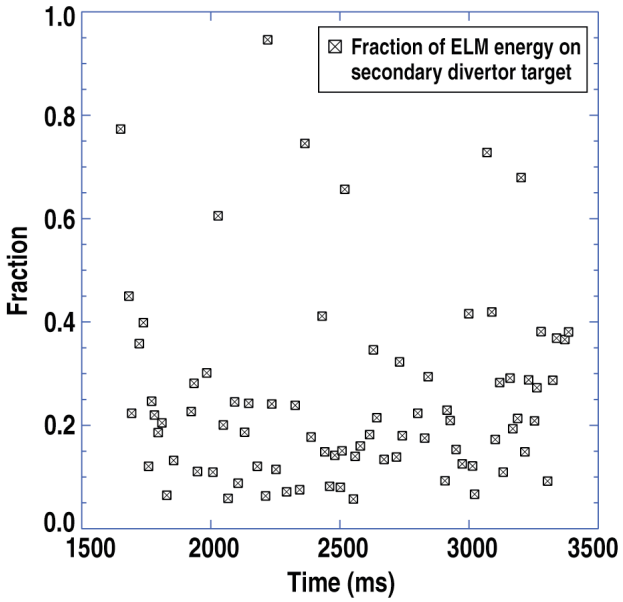

FIG. 9. The fraction shown is the secondary divertor target energy/core ELM energy loss for all of the ELMs in shot 142217 between 1500 and 3500 ms. The scatter in the points is due to the noise in the core ELM energy loss measurement.

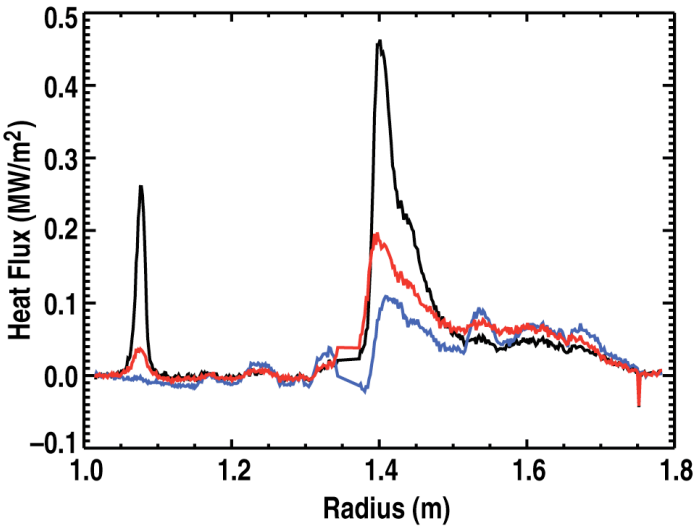

FIG. 10. This figure shows the effect of increasing DRSEP or increasing the density compared to the reference shot (black curve, DRSEP = 0.83 cm, density of 5.5×10^{19} m^{-3}). The red curve is at 33% higher density (7.5×10^{19} m^{-3}), slightly smaller dsrep (0.6 cm), and shows 44% less peak heat flux than the reference shot (black curve). The blue and black curves have the same density but the blue curve with 62% higher DRSEP (1.3 cm) shows 76% lower peak heat flux.

4. SUMMARY AND CONCLUSION

We show that the SOL width measured at the outboard midplane in IWL configuration is on average ~2.5 times larger than in LSN, confirming the assumptions used by ITER. The measured λ_q values show no correlation with the scaling trends as the plasma parameters change. With the exception of detached discharges and those affected by a proximity of the secondary limiter, the absolute measured values of λ_q agree with the scaling within the assumed uncertainty of a factor of 2. The fact that our results are in reasonable agreement with a scaling based on data from JT-60U and JET, machines with a considerably larger R, constitutes an approximate confirmation of the validity of the R^2 dependence in Eq. (1).

The secondary divertor study shows that the steady state heat flux profile can be predicted from the outboard midplane scrape-off layer thickness but the ELM heat flux pattern is more erratic. In steady state, about 5% of the SOL power is deposited in the secondary divertor for our ITER similar shape. A larger than expected fraction goes to the inner strike point and is mostly due to ELMs. The ELM deposited energy for the ITER similar shape is measured to be about 20% of the main plasma core energy loss but depends on DRSEP and density. The ELM heat flux deposition pattern can appear far away from the secondary divertor strike point. Further analysis may yield a more predictable pattern for the ELM energy deposition but it currently appears that most of the heat is deposited between ELMs near the secondary divertor strike point and during ELMs in the far SOL and at the inner strike point.

REFERENCES

[1] PITTS, R.A., et al., "Physics Basis and Design of the ITER Plasma-Facing Components." in Plasma Surface Interactions (Proc. 19th Intl. Conf. San Diego, 2010) submitted to J. Nucl. Mater.

[2] LOARTE, A., et al., Fusion Energy 2008 (Proc. 22nd Conf., Geneva, 2008), IAEA, Vienna, Paper IT/P6-13, http://www-pub.iaea.org/MTCD/Meetings/fec2008pp.asp

[3] STANGEBY, P.C., Nucl. Fusion **50**, 035013 (2010).

[4] KOCAN, M., and GUNN, J.P., Plasma Phys. Control. Fusion **52**, 045010 (2010).

[5] HERRMANN, A. , et al., Plasma Phys. Control. Fusion **37**, 17 (1995).

[6] LASNIER, C.J., "Scaling of divertor heat flux profile widths in DIII-D," these proceedings, EXD/P3-20.

ACKNOWLEDGMENT

This work was supported in part by the US Department of Energy under DE-AC04-94AL85000, DE-FG02-07ER54917, DE-AC52-07NA27344, DE-FC02-04ER54698, and the Collaborative Research Opportunities grant from the National Sciences and Engineering Research Council of Canada. Many Thanks to T. Osborne for help with the fast equilibrium analysis.